

Studies on the role of oxidative phosphorylation for mitochondrial antiviral innate immunity

吉住, 拓馬

<https://doi.org/10.15017/1931736>

出版情報 : 九州大学, 2017, 博士 (理学), 課程博士
バージョン :
権利関係 :

**Studies on the role of oxidative phosphorylation for
mitochondrial antiviral innate immunity**

Takuma Yoshizumi

Graduate School of Systems Life Sciences,

Kyushu University

2017

CONTENTS

	Page
ABBREVIATIONS	3
GENERAL INTRODUCTION	4
SUMMARY OF THE THESIS	6
BACKGROUND OF THE STUDY	7
RESULTS AND DISCUSSION	9
EXPERIMENTAL PROCEDURES	17
REFERENCES	26
ACKNOWLEDGEMENT	29
FIGURE LEGENDS	30
FIGURES	39

ABBREVIATIONS

ATeam; ATP indicator based on epsilon subunit for analytical measurements

ATP; adenosine 5'-triphosphate

BRET; bioluminescence resonance energy transfer

cGAS; cyclic GMP-AMP synthase

COX; cytochrome *c* oxidase

ETC; electron transport chain

FRET; fluorescence resonance energy transfer

IFN; interferon

I κ B α ; inhibitor of κ B α

IRF3; interferon regulatory factor 3

MAVS; mitochondrial antiviral signaling protein

MDA-5; melanoma differentiation-associated gene 5

mtDNA; mitochondrial DNA

ND1; NADH-ubiquinone oxidoreductase chain 1

NF- κ B; nuclear factor κ B

OPA1; optic atrophy 1

OXPPOS; oxidative phosphorylation

RIG-I; retinoic acid-inducible gene I

RRLR; RIG-I-like receptor

STING; stimulator of interferon genes

TLR; Toll-like receptor

GENERAL INTRODUCTION

Mitochondria are organelles in eukaryotic cells that have two respective membrane bilayers and original DNA (mitochondrial DNA; mtDNA). In live cells, mitochondria form tubular network and continuously undergo fusion and fission. This mechanism, called mitochondrial dynamics, is tightly connected with changes among the various functions of mitochondria, which include adenosine 5'-triphosphate (ATP) production by oxidative phosphorylation (OXPHOS)¹, apoptosis regulation², calcium homeostasis³ and so on.

In this decade, an additional role of mitochondria in innate immune response against RNA virus infection is focused. In mammals, viral RNAs are recognized by Toll-like receptors (TLRs) and RIG-I-like receptors (RLRs) and innate immune signaling is activated⁴. Mitochondria act as a platform of RLR pathway via mitochondrial antiviral signaling protein (MAVS)⁵. MAVS binds to retinoic acid inducible gene I or melanoma differentiation-associated gene 5 (RIG-I or MDA-5, i.e., RLRs), which recognize viral RNA in cytosol, and induces type I interferon and pro-inflammatory cytokines production⁶. Previous studies indicate that RLR pathway is up- or down-regulated by various factors. For example, mitochondrial membrane potential ($\Delta\Psi_m$) is required for RLR pathway activation⁷. $\Delta\Psi_m$ is the proton gradient across mitochondrial inner membrane created by respiratory activity and $\Delta\Psi_m$ dissipation causes the deficiency of OXPHOS activity and mitochondrial dysmorphology. However, it is not clear why RLR pathway is inactivated by

$\Delta\Psi_m$ dissipation. In this thesis, I focused on the role of OXPHOS activity for RLR pathway using variety of cultured cell lines.

(References)

1. Attardi, G. & Schatz, G. Biogenesis of mitochondria. *Annu. Rev. Cell Biol.* **4**, 289–333 (1988).
2. Wang, C. & Youle, R. J. The role of mitochondria in apoptosis. *Annu. Rev. Genet.* **43**, 95–118 (2009).
3. Leo, S., Bianchi, K., Brini, M. & Rizzuto, R. Mitochondrial calcium signalling in cell death. *FEBS J.* **272**, 4013–4022 (2005).
4. Meylan, E. & Tschopp, J. Toll-like receptors and RNA helicases: two parallel ways to trigger antiviral responses. *Mol. Cell* **22**, 561–569 (2006).
5. Seth, R. B., Sun, L., Ea, C. K. & Chen, Z. J. Identification and characterization of MAVS, a mitochondrial antiviral signalling protein that activates NF- κ B and IRF3. *Cell* **122**, 669–682 (2005).
6. Koshihara, T. Mitochondrial-mediated antiviral immunity. *Biochim. Biophys. Acta* **1833**, 225–232 (2013).
7. Koshihara, T., Yasukawa, K., Yanagi, Y. & Kawabata, S. Mitochondrial membrane potential is required for MAVS-mediated antiviral signalling. *Sci. Signal.* **4**, ra7 (2011).

SUMMARY OF THE THESIS

Mitochondria act as a platform for antiviral innate immunity, and the immune system depends on activation of the retinoic acid-inducible gene I (RIG-I)-like receptors (RLR) signaling pathway via an adaptor molecule, mitochondrial antiviral signaling. We report that RLR-mediated antiviral innate immunity requires oxidative phosphorylation (OXPHOS) activity, a prominent physiologic function of mitochondria. Cells lacking mitochondrial DNA or mutant cells with respiratory defects exhibited severely impaired virus-induced induction of interferons and pro-inflammatory cytokines. Recovery of the OXPHOS activity in these mutants, however, re-established RLR-mediated signal transduction. Studies to elucidate the molecular mechanism of OXPHOS-coupled immune activity revealed that optic atrophy 1, a mediator of mitochondrial fusion, contributes to regulate the antiviral immune response. Our findings provide evidence for functional coordination between RLR-mediated antiviral innate immunity and the mitochondrial energy generating system in mammals.

BACKGROUND OF THE STUDY

Innate immunity is a ubiquitous system that widely protects organisms from infectious pathogens as a front-line host defense mechanism. The immune response is triggered by the recognition of broadly conserved microbial components, known as pathogen-associated molecular patterns, by germline-encoded pattern recognition receptors of the host cells¹. As an early defense system against RNA viruses in mammals, the innate immune response is precisely controlled by two distinct signal transduction pathways mediated by the pattern recognition receptors Toll-like receptor 3 (TLR3) and retinoic acid-inducible gene I (RIG-I)-like receptors (RLRs) that respond to virus-derived RNAs^{2, 3} (i.e., pathogen-associated molecular patterns). Although the two pathways differ with respect to the initial activation of their downstream effectors, they converge at the point of activation of the transcriptional factors interferon regulatory factor 3 (IRF3) and nuclear factor κ B (NF- κ B), which results in the rapid production of type I interferons (IFN- α and - β) and other pro-inflammatory cytokines to establish adaptive antiviral immunity⁴. Mitochondria, eukaryotic cell powerhouses, are crucially involved in numerous cellular processes, including apoptosis⁵ and calcium homeostasis⁶. Mitochondria also have a unique role in innate immunity against RNA viruses⁷. Mitochondrial-mediated antiviral immunity depends on activation of the RLR signaling pathway, and mitochondrial antiviral signaling (MAVS), a downstream adaptor of RLR at the mitochondrial outer membrane (MOM),

has a key role in the signal transduction^{8,9}. Upon viral infection, MAVS recruits various types of effectors at the MOM, and the orchestrated “MAVS signalosome”, including the mitochondrial membrane potential ($\Delta\Psi_m$), is the primary unit governing antiviral innate immunity^{10,11}. Although the role of the MAVS signalosome in mitochondria with its dynamic morphologic properties¹² to provide a molecular platform that facilitates signal transduction is well characterized, insight into how the organelle functions to facilitate antiviral immunity through the activity of oxidative phosphorylation (OXPHOS) has remained unclear.

RESULTS AND DISCUSSION

Cultured cells rely on mitochondrial respiratory activity.

To evaluate the functional coordination of mitochondrial-mediated antiviral immunity and OXPHOS activity, we first sought to determine optimal cell culture conditions in which the cellular bioenergetics would rely on mitochondrial respiratory activity. We used a fluorescence resonance energy transfer (FRET)-based assay to visualize metabolized intracellular adenosine 5'-triphosphate (ATP) at the single-cell level in human embryonic kidney 293 (HEK293) cells expressing an ATP probe, ATeam1.03¹³. The biosensor assay performed with cells cultured under our customized medium containing galactose (10 mM) as the carbon source revealed high FRET signal [based on an emission ratio of 527/475 nm (denoted YFP/CFP)] in individual cells [Fig. 1A, galactose panels, (-)], indicating that cells maintained adequate intracellular ATP levels. The intracellular ATP level, however, which affects the YFP/CFP ratio, was dramatically decreased (~2.5-fold) by the addition of electron transport chain (ETC) inhibitors (rotenone and antimycin A), an ATP synthase inhibitor (oligomycin), or a protonophore [carbonyl cyanide *m*-chlorophenylhydrazone (CCCP)] to the media [Fig. 1A, galactose panels, (+), and B], demonstrating that energy production in the cells critically depends on mitochondrial OXPHOS. In contrast, cells maintained in a customized medium containing glucose (10 mM) exhibited no significant decrease in the intracellular ATP level, even after treatment with the pharmacologic

drugs (Fig. 1A, B). These results clearly demonstrated that the cellular bioenergetics are less dependent on OXPHOS activity in the presence of glucose, and that cellular ATP production predominantly relies on glycolysis.

Validation of the RLR signaling pathway under oxidative conditions.

We examined RLR-mediated signal transduction under the galactose-containing oxidative condition. Under oxidative conditions, similar to the glucose condition, ectopic expression of MAVS in HEK293 cells potently activated both IFN- β and NF- κ B luciferase reporters in a dose-dependent manner (Fig. 2A). The OXPHOS-dependent RLR-mediated signal transduction was also confirmed by stimulating cells transfected with either a plasmid encoding RIG-I (1–250) (Fig. 2B) or a synthetic analog of viral double-stranded RNA [dsRNA; poly(I:C)] (Fig. 2C and D), both of which are upstream factors of MAVS³. The kinetic response of IRF3 phosphorylation (a hallmark of IRF3 activation) in cells against infection by Sendai virus (SeV), a negative-stranded RNA virus of the *Paramyxoviridae* family, in the OXPHOS-dependent condition was also similar to that in the glucose condition (Fig. 3A). The RIG-I-mediated activation of the IFN- β reporter in the OXPHOS-dependent condition was sufficiently impaired by co-expression of a hepatitis C virus serine protease NS3/4A (an inhibitor of the RLR signaling pathway)^{14, 15} [Fig. 3B, wild-type (WT)], whereas its inactive mutant (S139A) had no functional

effect, indicating that the observed signal transduction occurred via RLR-dependent signaling pathway.

We next analyzed the structural features of MAVS activation accompanied by RLR-mediated signal transduction, homotypic oligomerization at the MOM¹¹, when cells were dependent on the oxidative condition. The interaction between ectopically expressed Venus- and NanoLuc luciferase (NLuc)-tagged MAVS with co-expression of the S139A mutant was successfully monitored, and a bioluminescence resonance energy transfer (BRET)-based assay¹⁶ revealed a hyperbolic saturation curve characteristic of a specific interaction (Fig. 3C, squares). Importantly, the specificity of the observed MAVS-MAVS interaction was verified by the disappearance of the saturated curve when the WT NS3/4A protease was co-expressed in cells due to MAVS cleavage¹⁴ (Fig. 3C, circles, also see immunoblot). We further verified the antiviral immune response of primary mouse embryonic fibroblasts (MEFs) against SeV infection in the OXPHOS-dependent condition. Gene expression profiling of MEFs revealed the expected induction of numerous IFN-stimulated and antiviral-signaling genes in response to the viral infection, similar to that observed in the glucose condition (Fig. 3D). Consistent with the aforementioned assays, we also observed that the antiviral immune response of macrophages cultured under the oxidative conditions was intensively upregulated upon SeV infection (Fig. 3E).

RLR-mediated antiviral innate immunity requires OXPHOS activity.

Because altering the energy metabolism in cells through the activity of OXPHOS could accomplish the antiviral immune response, we next asked whether arresting OXPHOS activity would disrupt RLR-mediated signal transduction. IRF3 phosphorylation in cells responding to SeV infection was completely suppressed by the addition of ETC inhibitors to the medium under oxidative conditions (Fig. 4A and B). The functionality of the cells treated with the pharmacologic drugs under these conditions, however, was unaffected when the cells were either stimulated with extracellular poly(I:C) (Fig. 4C) or infected with a double-stranded DNA virus, Herpes simplex virus 1 (HSV-1) (Fig. 4D), which activates the TLR3 or cGAS/STING cytosolic DNA sensing pathways, respectively. Influenza A virus (IAV; PR8 strain), an RNA virus of the *Orthomyxoviridae* family, encodes the viral protein PB1-F2 that translocates into mitochondria and induces mitochondrial depolarization¹⁷⁻²⁰. Using the viral strain, we observed severe PB1-F2-induced inhibition of RLR signaling in cells that depended on OXPHOS (Fig. 4E, WT); the inhibitory effect was attenuated, however, when we used a recombinant virus with genetic ablation of the PB1-F2 gene (Δ PB1-F2)²¹. These observations suggest that the severity of the mitochondrial dysfunction correlates with the severity of the defect in the RLR-induced antiviral response.

We next used a genetic approach to examine whether mitochondrial DNA (mtDNA),

which is essential for mitochondrial OXPHOS activity²², modulates RLR-mediated signal transduction. Mouse fibrosarcoma B82 cells devoid of mtDNA (ρ_0 B82)²³ (Fig. 5A) produced less IFN- β and IL-6 against SeV infection, although the immune response was fully rescued in a cell cybrid harboring WT mtDNA (Fig. 5B), despite the fact that both cell types had adequate energy due to the use of a high glucose medium (25 mM) with pyruvate and uridine (Fig. 5C) or the same infection level (Fig. 5D). Conversely, ρ_0 B82 cells had substantial antiviral responses against HSV-1 infection (Fig. 5E), consistent with a previous observation²⁴. To confirm that these observations were not due to specific characteristics of the cell type we used, we performed the same experiment in HeLa cells lacking mtDNA²⁵ (ρ_0 HeLa), and found that ρ_0 HeLa cells also exhibited defective antiviral innate immune responses against SeV infection (Fig. 5F). In addition, transient depletion of mtDNA in macrophages (mtDNA-less J774A.1) treated with rhodamine 6G exhibited an impaired immune response against SeV infection (Fig. 5G). Taken together, these findings indicated that RLR-mediated signal transduction requires OXPHOS activity to execute antiviral immune responses.

Pathogenic mtDNA mutations cause defects in antiviral innate immunity.

The importance of mtDNA in the regulation of RLR-mediated signal transduction prompted us to explore the phenotypic effects of pathogenic mtDNA mutations on antiviral

immunity. We used human osteosarcoma cybrid 143B cells harboring homoplasmic pathogenic mtDNA mutations: the ND1 cybrid²⁶ (complex I dysfunction), which is associated with Leber hereditary optic neuropathy, carrying a missense mutation at 3460/ND1; and the COX cybrid²⁷ (missing complex IV), which is associated with mitochondrial encephalopathy, carrying a stop codon mutation at 6930/COXI, both of which exhibit severe respiratory defects. As described, ρ_0 cells from 143B cell lines also exhibited an impaired immune response against SeV infection (Fig. 6A and B). Remarkably, activation of the RLR mediated antiviral signaling in the mutant cells (ND1 and COX) was severely disrupted (Fig. 6A and B) despite the indistinguishable MAVS pattern and energy supply (Fig. 6C, D and E). Consistent with these results, both pathogenic mutants were more susceptible to viral infection (recombinant IAV-expressing GFP)²⁸ than WT cells (Fig. 6F), due to defective mitochondrial-mediated immunity. Most importantly, the immunodeficiency observed in the ND1 cybrid, but not in the COX cybrid, was significantly recovered by the addition of succinate, a complex II substrate, to the media, suggesting that OXPHOS activity in ND1 mutant cells was driven by the substrate through complex II, which consequently restored its phenotype (Fig. 6G). Together, these results indicated that cells with defective OXPHOS activity due to mtDNA mutations have severely impaired RLR-mediated antiviral signaling.

OPA1-mediated execution of antiviral innate immunity.

To elucidate the molecular basis of OXPHOS activity coupled with the RLR signaling pathway, we speculated that optic atrophy 1 (OPA1), a mediator of mitochondrial fusion²⁹, has a role in antiviral innate immunity¹² because of its stabilizing effects on mtDNA³⁰ and the cristae structure^{31, 32}, both of which contribute to regulating mitochondrial respiration. As reported previously, we observed that *OPA1*^{-/-} cells contained less mtDNA (Fig. 7A), completely lacked mitochondrial fusion (Fig. 7B), and had a disrupted cristae morphology (Fig. 7C). These phenotypic defects were restored when a *WT OPA1* isoform gene (L-OPA1; variant 1), but not an inactive mutant *K301A* or short isoform (*S-OPA1*), was re-introduced into null cells. Strikingly, although the *OPA1*^{-/-} cells exhibited severely impaired SeV-induced production of IFN- β and IL-6 (Fig. 7D), the immune responses were substantially restored by recovery of the mtDNA level in rescued cells [Figs 7A, E; *VI(WT)*]. Given that OPA1 is important for mtDNA stability and the antiviral immune response, we used histochemical staining for cytochrome *c* oxidase (complex IV) activity to directly assess the OPA1 function involved in mitochondrial respiration. As expected, the COX staining pattern of the *VI(WT)*-rescued *OPA1*^{-/-} cells showed full recovery of the respiration defect, whereas *K301A* and *S-OPA1* failed to rescue the COX activities (Fig. 7F). Taken together, these results indicate that functional actions of OPA1 are linked to the improvement of OXPHOS activity and the induction of mitochondrial-mediated antiviral innate

immunity.

The findings of the present study using *in vitro* approaches provided new insight into how mitochondria facilitate antiviral immunity through OXPHOS activity. Mitochondria are believed to have evolved from organisms such as α -proteobacterium, and the discovery of their role in host-cell defense was unexpected. It is not surprising, however, that cells gaining respiratory function through a symbion could greatly advance not only through enhanced energy production, but also through safeguarded host defense against other infectious pathogens, especially in vertebrates.

EXPERIMENTAL PROCEDURES

Reagents

CCCP, rotenone, oligomycin, and antimycin A were purchased from Sigma-Aldrich (St. Louis, MO). Cytochrome *c* from horse heart was supplied by Nacalai Tesque Inc. (Kyoto, Japan) and 3,3'-diaminobenzidine was purchased from Tokyo Chemical Industry Co. Ltd. (Tokyo, Japan). Furimazine was supplied by Promega (Madison, WI) and poly(I:C) was purchased from InvivoGen (San Diego, CA). All other reagents were of biochemical research grade.

Antibodies

A polyclonal antibody against IRF3 (FL-425; 1:2000) and monoclonal antibody against β -actin (C4; 1:4000) were purchased from Santa Cruz Biotechnology (Dallas, TX), and the rabbit monoclonal antibody against phosphorylated IRF3 (p-IRF3) Ser386 (EPR2346; 1:2000) and polyclonal antibody against MAVS (ab25084; 1:1000) were from Abcam (Cambridge, MA). Monoclonal antibodies against Myc (9E10; 1:1000) and FLAG (M2; 1:1000) were obtained from Covance (Princeton, NJ) and Sigma-Aldrich, respectively. Monoclonal antibodies against phosphorylated I κ B α (p-I κ B α) Ser32/36 (5A5; 1:1000), phosphorylated NF- κ B p65 (p-NF- κ B p65) Ser536 (93H1; 1:2000) and NF- κ B p65 (D14E12; 1:3000) were supplied by Cell Signaling Technology (Danvers, MA), and the monoclonal antibody against OPA1 (1:2000) was from BD

Biosciences (San Jose, CA). Polyclonal antibody against SeV (PD029; 1:1000) was purchased from MBL (Nagoya, Japan). Monoclonal antibodies against mtCO1 (1D6E1A8; 1:1000) and mitochondrial heat shock protein 70 (mtHsp70; 1:2000) were purchased from Molecular Probes/Invitrogen (Carlsbad, CA) and Affinity BioReagents (Golden, CO), respectively. The Alexa Fluor 488–conjugated polyclonal antibody against rabbit immunoglobulin G (IgG) and Alexa Fluor 568–conjugated polyclonal antibody against rabbit IgG (1:500) were obtained from Molecular Probes-Invitrogen, and the Cy3-conjugated sheep anti-mouse IgG (1:1000) monoclonal antibody was purchased from Jackson ImmunoResearch Laboratories (West Grove, PA). A monoclonal antibody against PB1-F2 (A/PR8 strain; 1:10) was a kind gift from Viktor Wixler (Munster University Hospital Medical School).

Plasmids

Plasmids encoding human MAVS variants, hRIG-I (1–250), NS3/4A variants, and the ATeam1.03 were described previously^{13, 16, 20, 33}. Plasmid encoding rat OPA1 was a gift from Naotada Ishihara (Kurume University, Japan). To generate the retroviral expression constructs, each cDNA was recloned into the retroviral vector pMXs-Puro (Cell Biolabs, San Diego, CA). The retroviral expression vectors were then transfected into the platinum packaging cell lines (Cell Biolabs), and the retroviral supernatant was harvested 48 h post-transfection and used to

infect cells.

Cell lines and viruses

HEK293, MEF, and J774A.1 cells were maintained in Dulbecco's modified Eagle medium (high glucose; 4,500 mg/L; GIBCO BRL) supplemented with 1% GlutaMAX, penicillin (100 U/ mL)-streptomycin (100 µg/mL), and 10% fetal bovine serum at 5% CO₂ and 37 °C. The ρ₀ cells (lacking mtDNA) from HeLa, B82 (mouse fibrosarcoma), and 143B (human osteosarcoma) and its WT or mutant mtDNA cybrids were similarly maintained, except with the addition of sodium pyruvate (110 mg/L) and uridine (50 µg/mL; ρ₀ medium). The mtDNA-less J774A.1 macrophages were pretreated with rhodamine 6 G (0.06 µg/mL in ρ₀ medium) for 48 h to transiently eliminate endogenous mtDNA. For glucose-free culture experiments, glycolytic (glucose) and oxidative (galactose) media were customized according to previously published protocols³⁴ with slight modifications; the glycolytic medium was distinct from the high glucose medium used to maintain the cultures. The customized medium was based on glucose and glutamine-free Dulbecco's modified Eagle medium (GIBCO; A14430-01) externally supplemented with 10% dialyzed fetal bovine serum (GIBCO; 26400-044), 2% GlutaMAX, penicillin (100 U/mL)-streptomycin (100 µg/mL), and either 10 mM glucose (glycolytic) or 10 mM galactose (oxidative), respectively. Sendai virus Cantell strain was purchased from the

American Type Culture Collection, and the recombinant influenza viruses A/PR8 (Δ PB1-F2)²¹ and IAV-GFP²⁸ were a generous gift from Jonathan A. McCullers (St. Jude Children's Research Hospital) and Adolfo García-Sastre (Icahn School of Medicine at Mount Sinai), respectively.

Luciferase assays

HEK293 cells were plated in 24-well plates (2.5×10^5 cells per well) in the customized media. The following day, the cells were co-transfected with 100 ng luciferase reporter plasmid (p125luc or pELAM), 2.5 ng *Renilla* luciferase internal control vector phRL-TK (Promega), and each of the indicated expression plasmids with Lipofectamine 2000 reagent (Invitrogen). Empty vector [pcDNA3.1(-)] was used to maintain equivalent amounts of DNA in each well. Cells were harvested 24 h after transfection and analyzed by a dual-luciferase reporter assay on the GloMax 20/20n luminometer (Promega). Each experiment was repeated at least three times.

BRET assay

All BRET saturation assays were performed as previously described¹⁶ with slight modifications. In brief, HEK293 cells (5×10^5 cells per well) cultured under customized media were co-transfected with a constant amount (5 ng) of NLuc-tagged MAVS plasmid and increasing amounts of Venus-tagged MAVS constructs using Lipofectamine 2000 reagent. Empty vector

[pcDNA3.1(-)] was used to maintain equivalent amounts of DNA in each well. The cells were harvested at 21 h post-transfection and transferred to each well of white 96-well microplates. NLuc substrate (furimazine; 5 μ M) was added, and the plates were analyzed via a BRET saturation assay using a Flexstation 3 Microplate Reader (Molecular Devices, Sunnyvale, CA) at 37 °C.

Enzyme-linked immunosorbent assay (ELISA)

Production of IFN- β was measured with species-specific ELISA reagents for human and murine IFN- β from Kamakura Techno-Science Inc. (Kanagawa, Japan) and PBL Biomedical Laboratories (Piscataway, NJ), respectively. Human and murine IL-6 were measured using specific paired antibodies from eBioscience.

Microarray analysis

Total RNA was isolated from each cultured condition of primary MEFs using TRIzol Reagent (Invitrogen) and purified using SV Total RNA Isolation System (Promega) according to the manufacturer's protocol. RNA samples were quantified using an ND-1000 spectrophotometer (NanoDrop Technologies, Wilmington, DE) and the quality was confirmed with an Experion System (Bio-Rad Laboratories, Hercules, CA). The cRNA was amplified, labeled (Low Input

Quick Amp Labeling Kit), and hybridized to the SurePrint G3 Mouse Gene Expression 8 × 60 K microarray according to the manufacturer's instructions (Agilent Technologies, Santa Clara, CA). All hybridized microarray slides were scanned by an Agilent scanner (Agilent Technologies). Relative hybridization intensities and background hybridization values were calculated using Agilent Feature Extraction Software (9.5.1.1). Raw signal intensities and flags for each probe were calculated from the hybridization intensities (gProcessedSignal), and spot information (gIsSaturated, etc.), according to the procedures recommended by Agilent. The raw signal intensities of four samples were normalized by a quantile algorithm with the 'preprocessCore' library package³⁵ of the Bioconductor software³⁶. To identify upregulated or downregulated genes, we calculated the Z-scores³⁷ and ratios (non-log scaled fold-change) from the normalized signal intensities of each probe to compare between control and experiment samples, and established criteria for regulated genes: Z-score ≥ 2.0 and ratio ≥ 1.5 -fold for upregulated genes, and Z-score ≤ -2.0 and ratio ≤ 0.66 for downregulated genes, respectively.

Visualization of cytoplasmic ATP in living cells

Imaging of cytoplasmic ATP levels in living cells was performed as previously described^{13,38}. Briefly, cells expressing ATeam1.03 were plated on collagen-coated 35-mm glass-bottom dishes (MatTek, Ashland, MA). The following day, the cells were washed once with the

customized media and the cells were subjected to ATP imaging. Observations of cells that were maintained at 5% CO₂ and 37 °C using a stage-top incubator (Tokai Hit, Shizuoka, Japan) were performed using a Nikon ECLIPSE Ti-E microscope with an oil-immersion type CFI Plan Apo VC 60x lens (Nikon Instruments Inc, Tokyo, Japan). The filters, 438/24-nm BrightLine single-band bandpass filter (FF01-438/24-25), 458-nm edge BrightLine single-edge dichroic mirror (FF458-Di02), and two emission filters (FF01-483/32 and FF01-542/27) used for dual-emission ratio imaging of ATeam1.03 were obtained from Semrock Inc. (Rochester, NY). Fluorescence emission from the ATeam1.03 was imaged by altering the emission filters with a filter changer and a scientific CMOS camera (Zyla 4.2, Andor Technology), and the imaging analysis was performed using MetaMorph (Molecular Devices). The YFP/CFP emission ratio was calculated by dividing the YFP intensity by the CFP intensity of each cell.

Confocal microscopy

Cells were plated on coverslips in 12-well plates (1.5×10^5 cells per well). The following day, cells were fixed with 4% paraformaldehyde for 10 min, permeabilized with 0.2% Triton X-100 in PBS (pH 7.4), and blocked with 5% bovine calf serum. Endogenous MAVS was detected with the polyclonal primary and Alexa Fluor 488 secondary antibodies, and mitochondria were stained with anti-mtHsp70 primary antibody followed by the Cy3-conjugated secondary antibody.

Cells were imaged with the C2⁺ confocal microscope (Nikon Instruments Inc).

Electron microscopy analysis

For electron microscopy, cells were fixed in 100 mM cacodylate buffer (pH 7.4) containing 2% paraformaldehyde and 2% glutaraldehyde (GA) for 1 h, washed and fixed again with 100 mM cacodylate buffer containing 2% GA overnight at 4 °C. After fixation, the cells were washed four times with 100 mM cacodylate buffer for 20 min each, and post-fixed with 2% osmium tetroxide (OsO₄) in cacodylate buffer at 4 °C for 1 h. Cells were then dehydrated in a graded series of ethanol (50%, 70%, 90%, and 100%), embedded in resin (Quetol 812, Nisshin EM Co., Japan), and polymerized at 60 °C for 48 h. The polymerized resins were cut in ultra-thin sections at 70 nm with an LEICA UTC ultramicrotome, mounted on copper grids, and stained with 2% uranyl acetate and lead solution (Sigma-Aldrich). Images were collected with a transmission electron microscope (JEM-1400Plus; JEOL Ltd, Japan) operating at 80 kV and equipped with a CCD camera (VELETA; Olympus Soft Imaging Solutions GmbH, Germany).

Quantification of mtDNA

Total genomic DNA was extracted and purified from cells, and diluted to 5 ng/μL. To quantify the amount of mtDNA per nuclear DNA, quantitative real-time polymerase chain

reaction (qPCR) was performed using FastStart Essential DNA Green Master (Roche). Quantification of relative copy number differences was performed based on the difference in the threshold amplification between mtDNA and nuclear DNA [$\Delta\Delta C(t)$ method]. We used the following sets of primers for mtDNA: TK702 (5'-cctatcaccttgccatcat, forward) and TK703 (5'-gaggctgttgcttggtgac, reverse); and for nuclear DNA: TK704 (5'-atggaaagcctgccatcatg, forward) and TK705 (5'-tccttggttcagcatcac, reverse).

Cytochemical analysis of cytochrome *c* oxidase (COX) activity

COX staining was performed as previously described³⁹ with slight modifications. MEFs plated on 18-mm coverslips were fixed with 2% paraformaldehyde in PBS for 15 min and washed twice with PBS for 5 min each. To visualize COX activity, cells were stained with 100 mM phosphate buffer (pH 7.4) containing 0.6 mg/mL 3',3'-diaminobenzidine, 0.3 mg/mL cytochrome *c*, and 45 mg/mL sucrose at 37 °C for 2 h. Cells were then washed twice with 0.1 M Tris-HCl buffer (pH 8.0) for 5 min each and analyzed by microscopy.

Statistical analysis

An analysis of variance test (GraphPad QuickCalcs) was used for the statistical analyzes. A *P*-value of less than 0.05 was considered statistically significant.

REFERENCES

1. Hoffmann, J. A., Kafatos, F. C., Janeway, C. A. Jr. & Ezekowitz, R. A. B. Phylogenetic perspectives in innate immunity. *Science* **284**, 1313–1318 (1999).
2. Kawai, T. & Akira, S. Innate immune recognition of viral infection. *Nat. Immunol.* **7**, 131–137 (2006).
3. Meylan, E. & Tschopp, J. Toll-like receptors and RNA helicases: two parallel ways to trigger antiviral responses. *Mol. Cell* **22**, 561–569 (2006).
4. Iwasaki, A. & Medzhitov, R. Regulation of adaptive immunity by the innate immune system. *Science* **327**, 291–295 (2010).
5. Wang, C. & Youle, R. J. The role of mitochondria in apoptosis. *Annu. Rev. Genet.* **43**, 95–118 (2009).
6. Rizzuto, R., De Stefani, D., Raffaello, A. & Mammucari, C. Mitochondria as sensors and regulators of calcium signalling. *Nat. Rev. Mol. Cell Biol.* **13**, 566–578 (2012).
7. Seth, R. B., Sun, L., Ea, C. K. & Chen, Z. J. Identification and characterization of MAVS, a mitochondrial antiviral signalling protein that activates NF- κ B and IRF3. *Cell* **122**, 669–682 (2005).
8. Kumar, H. *et al.* Essential role of IPS-1 in innate immune responses against RNA viruses. *J. Exp. Med.* **203**, 1795–1803 (2006).
9. Sun, Q. *et al.* The specific and essential role of MAVS in antiviral innate immune responses. *Immunity* **24**, 633–642 (2006).
10. West, A. P., Shadel, G. S. & Ghosh, S. Mitochondria in innate immune responses. *Nat. Rev. Immunol.* **11**, 389–402 (2011).
11. Koshiha, T. Mitochondrial-mediated antiviral immunity. *Biochim. Biophys. Acta* **1833**, 225–232 (2013).
12. Castanier, C., Garcin, D., Vazquez, A. & Arnoult, D. Mitochondrial dynamics regulate the RIG-I-like receptor antiviral pathway. *EMBO Rep.* **11**, 133–138 (2010).
13. Imamura, H. *et al.* Visualization of ATP levels inside single living cells with fluorescence resonance energy transfer-based genetically encoded indicators. *Proc. Natl. Acad. Sci. USA* **106**, 15651–15656 (2009).
14. Li, X. D., Sun, L., Seth, R. B., Pineda, G. & Chen, Z. J. Hepatitis C virus protease NS3/4A cleaves mitochondrial antiviral signaling protein off the mitochondria to evade innate immunity. *Proc. Natl. Acad. Sci. USA* **102**, 17717–17722 (2005).
15. Meylan, E. *et al.* Cardif is an adaptor protein in the RIG-I antiviral pathway and is targeted by hepatitis C virus. *Nature* **437**, 1167–1172 (2005).
16. Sasaki, O. *et al.* A structural perspective of the MAVS-regulatory mechanism on the

- mitochondrial outer membrane using bioluminescence resonance energy transfer. *Biochim. Biophys. Acta* **1833**, 1017–1027 (2013).
17. Chen, W. *et al.* A novel influenza A virus mitochondrial protein that induces cell death. *Nat. Med.* **7**, 1306–1312 (2001).
 18. Gibbs, J. S., Malide, D., Hornung, F., Bennink, J. R. & Yewdell, J. W. The influenza A virus PB1-F2 protein targets the inner mitochondrial membrane via a predicted basic amphipathic helix that disrupts mitochondrial function. *J. Virol.* **77**, 7214–7224 (2003).
 19. Zamarin, D., Garcia-Sastre, A., Xiao, X., Wang, R. & Palese, P. Influenza virus PB1-F2 protein induces cell death through mitochondrial ANT3 and VDAC1. *PLoS Pathog.* **1**, e4 (2005).
 20. Yoshizumi, T. *et al.* Influenza A virus protein PB1-F2 translocates into mitochondria via Tom40 channels and impairs innate immunity. *Nat. Commun.* **5**, 4713 (2014).
 21. McAuley, J. L. *et al.* Expression of the 1918 Influenza A virus PB1-F2 enhances the pathogenesis of viral and secondary bacterial pneumonia. *Cell Host Microbe* **2**, 240–249 (2007).
 22. Attardi, G. & Schatz, G. Biogenesis of mitochondria. *Annu. Rev. Cell Biol.* **4**, 289–333 (1988).
 23. Inoue, K. *et al.* Isolation and characterization of mitochondrial DNA-less lines from various mammalian cell lines by application of an anticancer drug, ditercalinium. *Biochem. Biophys. Res. Commun.* **239**, 257–260 (1997).
 24. West, A. P. *et al.* Mitochondrial DNA stress primes the antiviral innate immune response. *Nature* **520**, 553–557 (2015).
 25. Hayashi, J. *et al.* Introduction of disease-related mitochondrial DNA deletions into HeLa cells lacking mitochondrial DNA results in mitochondrial dysfunction. *Proc. Natl. Acad. Sci. USA* **88**, 10614–10618 (1991).
 26. Baracca, A. *et al.* Severe impairment of complex I-driven adenosine triphosphate synthesis in leber hereditary optic neuropathy cybrids. *Arch. Neurol.* **62**, 730–736 (2005).
 27. D’Aurelio, M., Gajewski, C. D., Lenaz, G. & Manfredi, G. Respiratory chain supercomplexes set the threshold for respiration defects in human mtDNA mutant cybrids. *Hum. Mol. Genet.* **15**, 2157–2169 (2006).
 28. Manicassamy, B. *et al.* Analysis of *in vivo* dynamics of influenza virus infection in mice using a GFP reporter virus. *Proc. Natl. Acad. Sci. USA* **107**, 11531–11536 (2010).
 29. Chen, H., Chomyn, A. & Chan, D. C. Disruption of fusion results in mitochondrial heterogeneity and dysfunction. *J. Biol. Chem.* **280**, 26185–26192 (2005).
 30. Chen, H. *et al.* Mitochondrial fusion is required for mtDNA stability in skeletal muscle and tolerance of mtDNA mutations. *Cell* **141**, 280–289 (2010).

31. Cogliati, S. *et al.* Mitochondrial cristae shape determines respiratory chain supercomplexes assembly and respiratory efficiency. *Cell* **155**, 160–171 (2013).
32. Patten, D. A. *et al.* OPA1-dependent cristae modulation is essential for cellular adaptation to metabolic demand. *EMBO J.* **33**, 2676–2691 (2014).
33. Yasukawa, K. *et al.* Mitofusin 2 inhibits mitochondrial antiviral signaling. *Sci. Signal.* **2**, ra47 (2009).
34. Mishra, P., Carelli, V., Manfredi, G. & Chan, D. C. Proteolytic cleavage of Opa1 stimulates mitochondrial inner membrane fusion and couples fusion to oxidative phosphorylation. *Cell Metab.* **19**, 630–641 (2014).
35. Bolstad, B. M., Irizarry, R. A., Astrand, M. & Speed, T. P. A comparison of normalization methods for high density oligonucleotide array data based on variance and bias. *Bioinformatics* **19**, 185–193 (2003).
36. Gentleman, R. C. *et al.* Bioconductor: open software development for computational biology and bioinformatics. *Genome Biol.* **5**, R80 (2004).
37. Quackenbush, J. Microarray data normalization and transformation. *Nat. Genet.* **32**, 496–501 (2002).
38. Hidaka, M. *et al.* Visualization of NO₃⁻/NO₂⁻ dynamics in living cells by fluorescence resonance energy transfer (FRET) imaging employing a rhizobial two-component regulatory system. *J. Biol. Chem.* **291**, 2260–2269 (2016).
39. Ishihara, T. *et al.* Dynamics of mitochondrial DNA nucleoids regulated by mitochondrial fission is essential for maintenance of homogeneously active mitochondria during neonatal heart development. *Mol. Cell. Biol.* **35**, 211–223 (2015).
40. Saeed, A. I. *et al.* TM4: a free, open-source system for microarray data management and analysis. *BioTechniques* **34**, 374–378 (2003).

ACKNOWLEDGEMENT

Studies in this thesis had been proceeded under the directions of Dr. Takumi Koshihara. I am grateful for Drs. Thomas Langer (University of Cologne), Katsuyoshi Mihara (Kyushu University), Hiromi Imamura (Kyoto University), Kazuto Nakada, Kaori Ishikawa, Michiyasu Kato (University of Tsukuba) and Yuichi Michikawa (National Institute of Radiological Sciences, Japan) for helpful discussions and valuable comments about this study. I appreciate to Yuko Fuchigami for her technical assistance with DNA cloning and sequencing and Norio Sasaoka for establishing ATeam1.03 expressing cell line and technical comments on the figure preparation. I am also thankful to technical support regarding the fluorescence measurements (BRET assay) from the Research Support Center, Graduate School of Medical Sciences, Kyushu University. The 143B COX and ND1 cybrids were a generous gift from Drs. Giovanni Manfredi (Cornell University) and Valerio Carelli (University of Bologna, Italy), respectively, and *OPA1*-null MEFs were obtained from Dr. David Chan (HHMI and Caltech).

Finally, I would like to show my appreciation to my parents and friends for encouraging and sustaining me during this study.

FIGURE LEGENDS

Figure 1. Bioenergetic profiling of cells under oxidative conditions.

(A) HEK293 cells stably expressing the ATeam1.03 were cultured in customized media containing either galactose (right) or glucose (left) at 37 °C, and then the indicated mitochondrial inhibitors were added to each medium. The time-course of the fluorescence emission ratio (YFP/CFP) was monitored to visualize cytosolic ATP levels in each living cell, and ratiometric pseudocolor images of cells pre- (–) or post-treated (+) with inhibitors are shown. The images were processed in MetaMorph (Molecular Devices), and the blue color indicates less cytoplasmic ATP. Scale bar, 20 μm.

(B) Quantification of the YFP/CFP ratio calculated from images in (A). Number of cells (*n*) used for the quantification is shown at the top of the graph. Error bars indicate S.D. (Unpaired *t*-test; ****P* < 0.001).

Figure 2. RLR-mediated signal transduction in HEK293 cells under oxidative conditions.

(A) Galactose-cultured HEK293 cells were transfected with empty vector (Mock) or increasing amounts (10, 20, 50 ng) of plasmids encoding MAVS, and with either IFN-β (left) or NF-κB (right) reporter plasmids. The transfected cells were analyzed 24 h later for reporter gene-dependent luciferase activities. Inset panel: glucose-cultured HEK293 cells (black bars) were also

tested as the control (50 ng MAVS plasmids) ($n = 3$).

(B, C) Similar to (A), except that HEK293 cells were transfected with either (B) RIG-I (1-250) or (C) poly(I:C) in a dose-dependent manner (10, 20, 50 ng) together with the IFN- β reporter plasmid. Inset panel: glucose-cultured HEK293 cells (black bars) were also tested as the control ($n = 3$).

(D) Similar to (C), except that HEK293 cells were transfected with either empty (Mock) or poly(I:C) (5 or 10 μ g), and the cell-free supernatant was collected for measurement of IFN- β production by ELISA. Inset panel: glucose-cultured HEK293 cells (black bar) were also tested as the control [10 μ g of poly(I:C)] ($n = 3$).

Error bars indicate S.D. (Unpaired t -test; $**P < 0.01$ and $***P < 0.001$, respectively). N.D., not detected in the experiment.

Figure 3. RLR-mediated signal transduction under oxidative conditions.

(A) The kinetic profile of IRF3 activation in oxidative or glycolytic medium-cultured HEK293 cells that were challenged with SeV (4 HA units/mL). Each cell lysate was collected at the indicated time-points (3, 6, 9 and 12 h) and analyzed by Western blotting with antibodies against the specific antibody (p-IRF3; phosphorylation of Ser386). Anti- β -actin was used as the loading control and anti-SeV as the infection control. U.I., uninfected.

(B) Oxidative-medium cultured HEK293 cells were transfected with 50 ng of empty vector (Mock) or expression plasmid for Myc-tagged RIG-I (1–250) (control) together with the IFN- β reporter plasmid. The two right lanes (+NS3/4A) indicate that 100 ng of FLAG-tagged WT or inactive (S139A) NS3/4A serine protease expression plasmids were also co-transfected with the RIG-I (1–250) plasmid. The immunoblot on the top represents an expression profile of Myc-tagged RIG-I (1–250) and FLAG-tagged NS3/4A mutants as well as the loading control of endogenous β -actin. Error bars indicate S.D. ($n = 3$; Unpaired t -test; ** $P < 0.01$ and *** $P < 0.001$, respectively).

(C) BRET saturation assay of MAVS oligomerization in glycolytic versus oxidative media. HEK293 cells were co-transfected with 5 ng NLuc-MAVS expression plasmid and increasing amounts (0–200 ng) of Venus-tagged MAVS plasmid along with 200 ng of WT (circles) or S139A (squares) FLAG-tagged NS3/4 A plasmids, and analyzed 24 h later using a BRET saturation assay. Closed and open symbols represent glycolytic and oxidative conditions of HEK293 cells, respectively, and inset blots show Western blots from the BRET saturation point of each curve by immunoblotting with the indicated antibodies. Error bars indicate S.E.M. ($n = 3$).

(D) Heat maps of microarray analysis. Total RNAs were isolated from glycolytic and oxidative cultured conditions of primary MEFs that were unchallenged (–) or challenged (+) with SeV (30 HA units/mL) for 6 h, and microarray analysis was performed. The heat map was generated by

MeV software⁴⁰, and the color indicates the distance from the median of each row.

(E) Similar to (A), except that J774A.1 macrophages were challenged with SeV (2 HA units/mL).

U.I., uninfected.

Figure 4. OXPHOS activity couples with the RLR pathway to execute antiviral signal transduction, but not TLR3 or cGAS/STING pathway.

(A) HEK293 cells cultured in glycolytic or oxidative media were infected with SeV (4 HA units/mL) for 2.5 h, and the infected cells were further incubated with the indicated mitochondrial inhibitors for 2.5 h (total 5 h infection). The activation of endogenous IRF3 was analyzed by Western blotting with antibodies against the specific antibody (p-IRF3; Ser386). Anti- β -actin was used as the loading control. U.I., uninfected.

(B) HEK293 cells cultured in glycolytic or oxidative media (incubated with indicated mitochondrial inhibitors) were infected with SeV (4 HA units/mL) for 5 h, and total RNAs from cells were analyzed by RT-PCR to detect viral infection. A region of the SeV *NP gene* (138-386) was amplified and *CLSI* was used as a loading control. U.I., uninfected.

(C) HEK293 cells stably expressing TLR3 and cultured in oxidative medium were stimulated with extracellular poly(I:C) (5 μ g) and the indicated mitochondrial inhibitors for 5 h. Activation of endogenous IRF3 was analyzed by Western blotting with antibodies against the specific

antibody (p-IRF3; phosphorylation of Ser386). Anti- β -actin was used as the loading control. U.T., untreated.

(D) Similar to (C), except that HEK293 cells stably expressing both cGAS and STING were infected with HSV-1 (5×10^4 PFU, total 12 h infection). U.I., uninfected.

(E) Comparison of the IRF3 activation between cells infected with recombinant influenza A/PR8 viruses (WT versus Δ PB1-F2, each used 2 HA units/mL) cultured under oxidative conditions. The Δ PB1-F2 strain is a mutant strain with genetic removal of the PB1-F2 gene from the viral genome²¹. The graph on the right shows the quantification of p-IRF3 bands analyzed by densitometry. Error bars indicate S.D. ($n = 3$; Unpaired t -test; $*P < 0.05$).

Figure 5. Defective RLR pathway in mtDNA-depleted cells.

(A) Comparison of COX activity between B82 WT cybrids and ρ_0 cells. Cells expressing COX activity were indicated by a brown color. Scale bar, 20 μ m.

(B) The B82 WT cybrids and ρ_0 cells were infected with SeV (4 HA units/mL) for 18 h and the cell-free supernatants were analyzed by ELISA to measure the secreted amounts of IFN- β (top panel) and IL-6 (bottom panel), respectively ($n = 3$).

(C) The B82 WT cybrids and ρ_0 cells were transfected with ATeam1.03-expressing plasmid. Cytoplasmic ATP levels in the cells were monitored 24 h post-transfection. The graph on the left

shows quantification of the YFP/CFP ratio calculated from analyzed images ($n = 19$ for WT and $n = 15$ for ρ_0 cells).

(D) The B82 WT cybrids and ρ_0 cells were infected with SeV (5 HA units/mL), and total RNAs from cells were analyzed by RT-PCR to detect viral infection. A region of the SeV *NP gene* (138-386) was amplified and *GAPDH* was used as a loading control.

(E) Similar to (B), the B82 WT cybrids and ρ_0 cells were infected with HSV-1 (1×10^5 PFU) for 24 h and the secreted amounts of IFN- β (top panel) and IL-6 (bottom panel) were analyzed by ELISA, respectively. ($n = 3$).

(F) The HeLa WT cybrids and ρ_0 cells were infected with SeV (5 HA units/mL) for 18 h, and activation of endogenous IRF3 and phosphorylation of I κ B α (p-I κ B α ; the hallmark of NF- κ B activation) were analyzed by Western blotting with specific antibodies.

(G) Similar to (B), except that the mtDNA-less J774A.1 and its parental macrophages were infected with SeV (2 HA units/mL). Inset panel: relative mtDNA copy number was confirmed by qPCR.

In all experiments, cells were maintained in ρ_0 medium. Error bars indicate S.D. (Unpaired *t*-test; N.S., not significant, $**P < 0.01$ and $***P < 0.001$, respectively). U.I., uninfected. N.D., not detected in the experiment.

Figure 6. Defects in mtDNA cause malfunction in antiviral innate immunity.

(A,B) The 143B cybrids and ρ_0 cells were infected with SeV (5 HA units/mL) for 18 h, and (A) activation of both IRF3 and $\text{I}\kappa\text{B}\alpha$ was analyzed by Western blotting with antibodies against its specific phosphorylated-detection antibodies (Ser386 for IRF3 and Ser32/36 for $\text{I}\kappa\text{B}\alpha$) or (B) the cell-free supernatants were analyzed by ELISA to measure the secreted amounts of IFN- β (left panel) and IL-6 (right panel) ($n = 3$). U.I., uninfected.

(C) Western blots revealed the abundance of endogenous MAVS in mtDNA mutant cells. Anti- β -actin was used as the loading control.

(D) Mitochondrial morphology and MAVS distribution (green) in mtDNA mutant cells (143B WT, ND1, and COX cybrids and its ρ_0 cells) were monitored by immunofluorescence microscopy. Mitochondria in the cells were stained with an anti-mtHsp70 monoclonal antibody (red). Scale bars, 10 μm .

(E) The time-course of the FRET signal of mtDNA mutant cells expressing ATeam1.03 was monitored to visualize the cytoplasmic ATP levels in each living cell. Scale bar, 20 μm . The graph on the right shows the quantification of the YFP/CFP ratio calculated from the images ($n = 17$ for WT, $n = 15$ for ND1, and $n = 10$ for COX).

(F) Fluorescence microscopy of 143B cybrid cells infected with IAV-GFP (0.5 HA units/mL) for 24 h. In (A–F), cells were maintained in ρ_0 medium.

(G) Similar to (B), except that succinate, the complex II substrate with ADP, was added to the oxidative medium as indicated ($n = 3$).

Error bars indicate S.D. (Unpaired t -test; N.S., not significant, $***P < 0.001$). N.D., not detected in the experiment.

Figure 7. OPA1 contributes to mitochondrial-mediated antiviral signaling through stabilizing mtDNA.

(A) Analysis of mtDNA copy number per nuclear DNA in WT and mutant MEFs. Restoration of mtDNA in *OPA1* null cells was measured in mutant cells infected with a retrovirus-expressing variant 1 WT *OPA1* [*VI(WT)*], its K301A mutant [*VI(K301A)*], and short isoform *OPA1* (*S-OPA1*). Error bars indicate S.E.M ($n = 3$; Unpaired t -test; $**P < 0.01$).

(B) Representative images of mitochondrial morphology in MEFs. The graph shows the quantification of the mitochondrial morphology in MEFs. Cells were scored (at least 300 cells) according to one of four morphologic categories, as shown in the inset. Error bars indicate S.D. Scale bar, 10 μm .

(C) The *WT*, *OPA1*^{-/-}, and its mutant *OPA1* gene re-introduced MEFs were analyzed by transmission electron microscopy. Scale bar, 1 μm .

(D) SeV-induced antiviral innate immune response in *OPA1*-null MEFs. The *WT* and *OPA1*-null

MEFs were either uninfected (U.I.) or infected with SeV (4 HA units/mL) for 18 h, and the cell-free supernatants were analyzed by ELISA to measure the secreted amounts of IFN- β (left panel) and IL-6 (right panel). Error bars indicate S.D. ($n = 3$; Unpaired t -test; ** $P < 0.01$ and *** $P < 0.001$, respectively). N.D., not detected in the experiment.

(E) Similar to (D), except that the immune response in mutant *OPAI* MEFs was monitored. Error bars indicate S.D. ($n = 3$; Unpaired t -test; *** $P < 0.001$).

(F) Cytochemical analysis of COX activity. Cells expressing COX activity were indicated by a brown color. Scale bar, 20 μm .

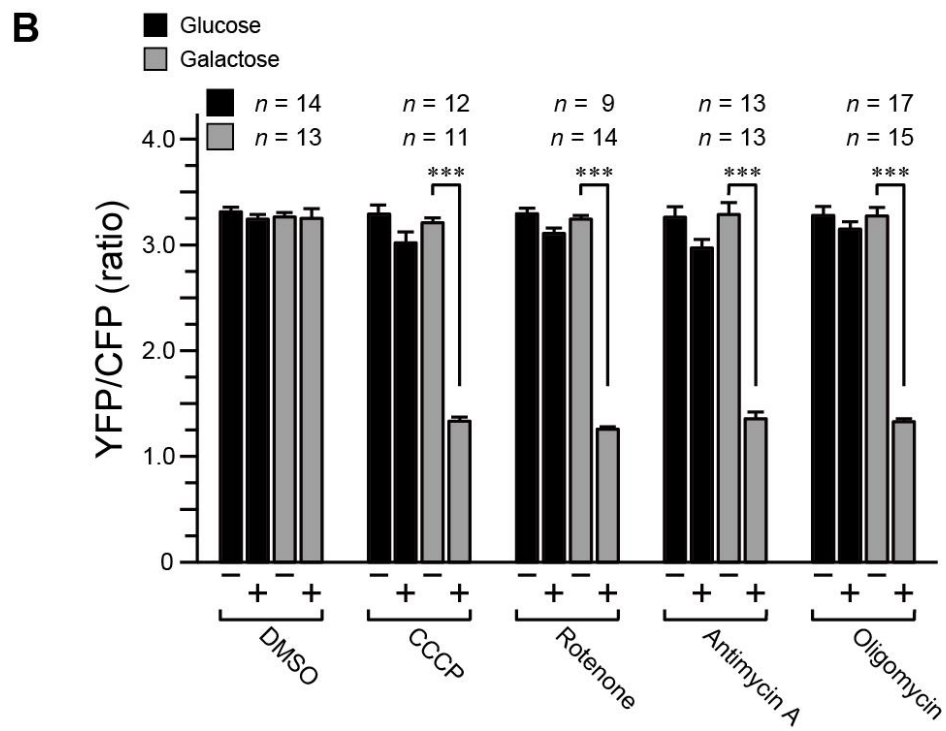
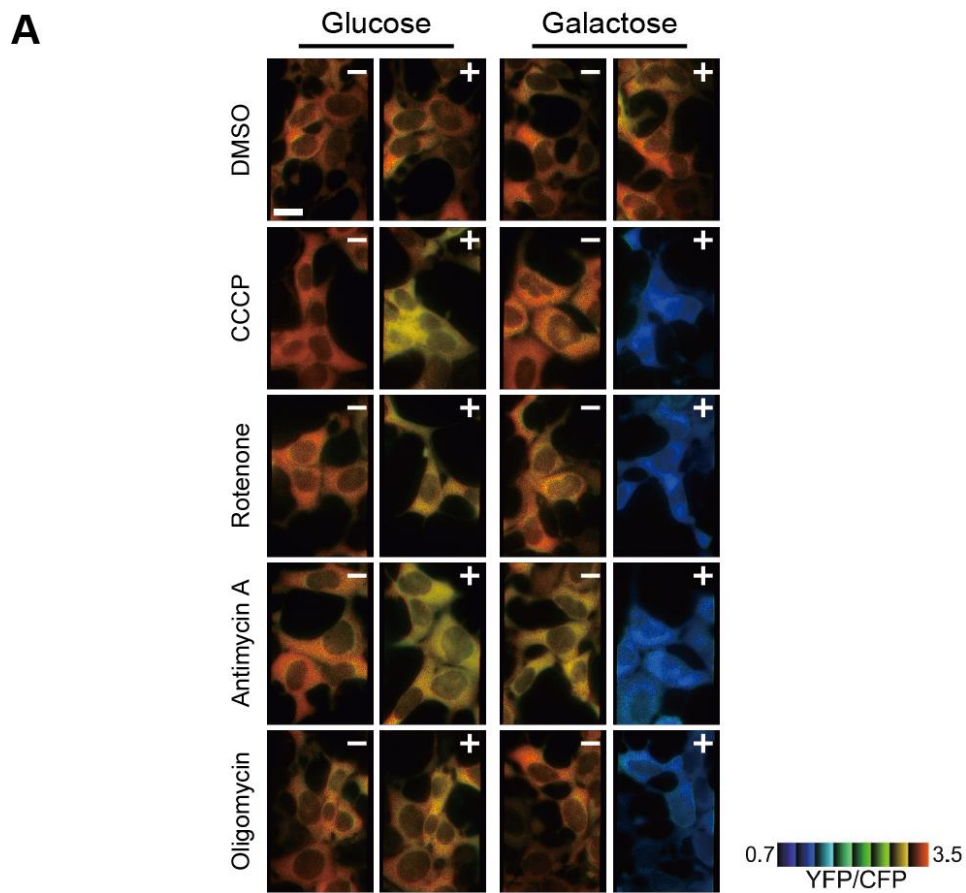


Figure 1

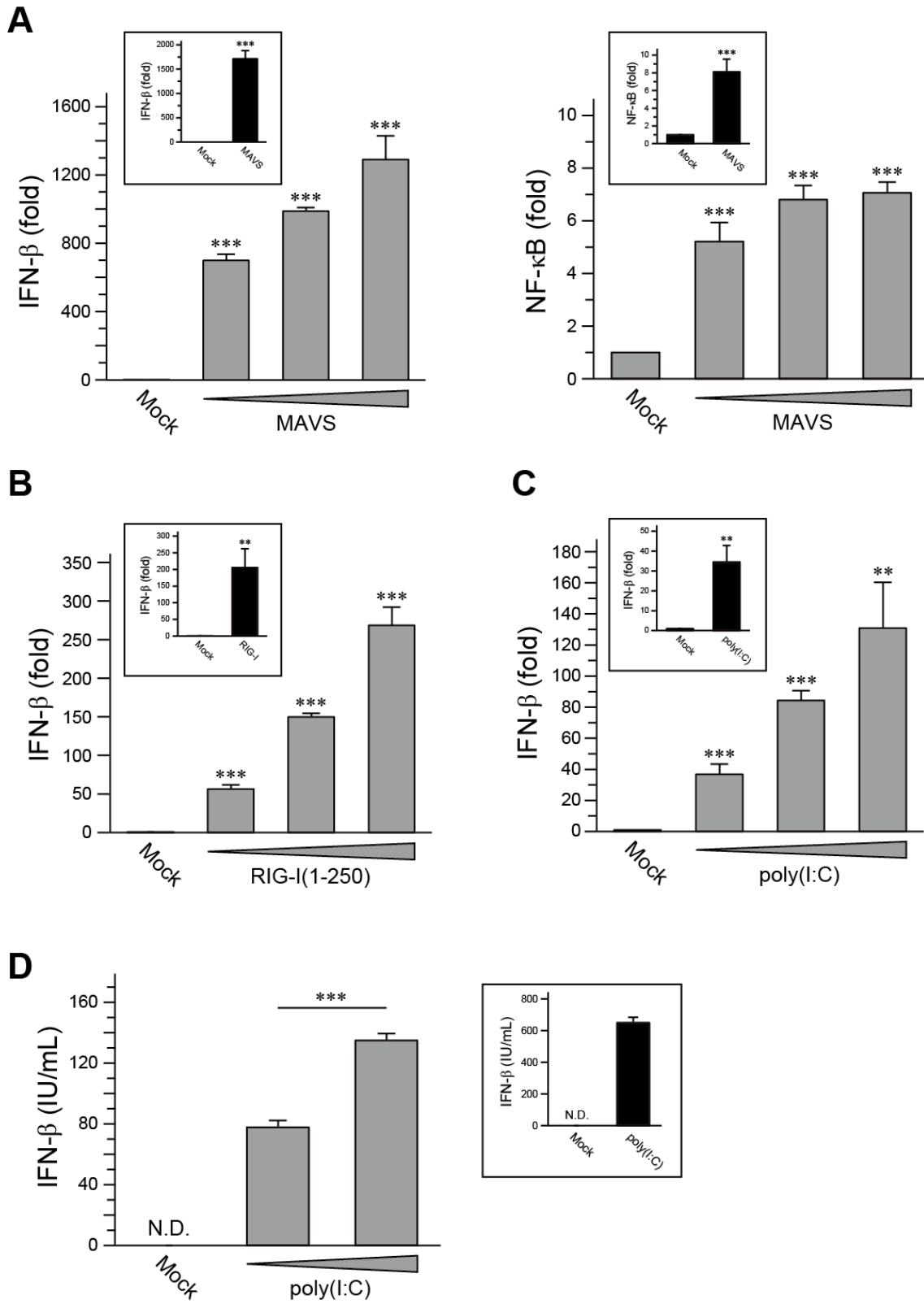


Figure 2

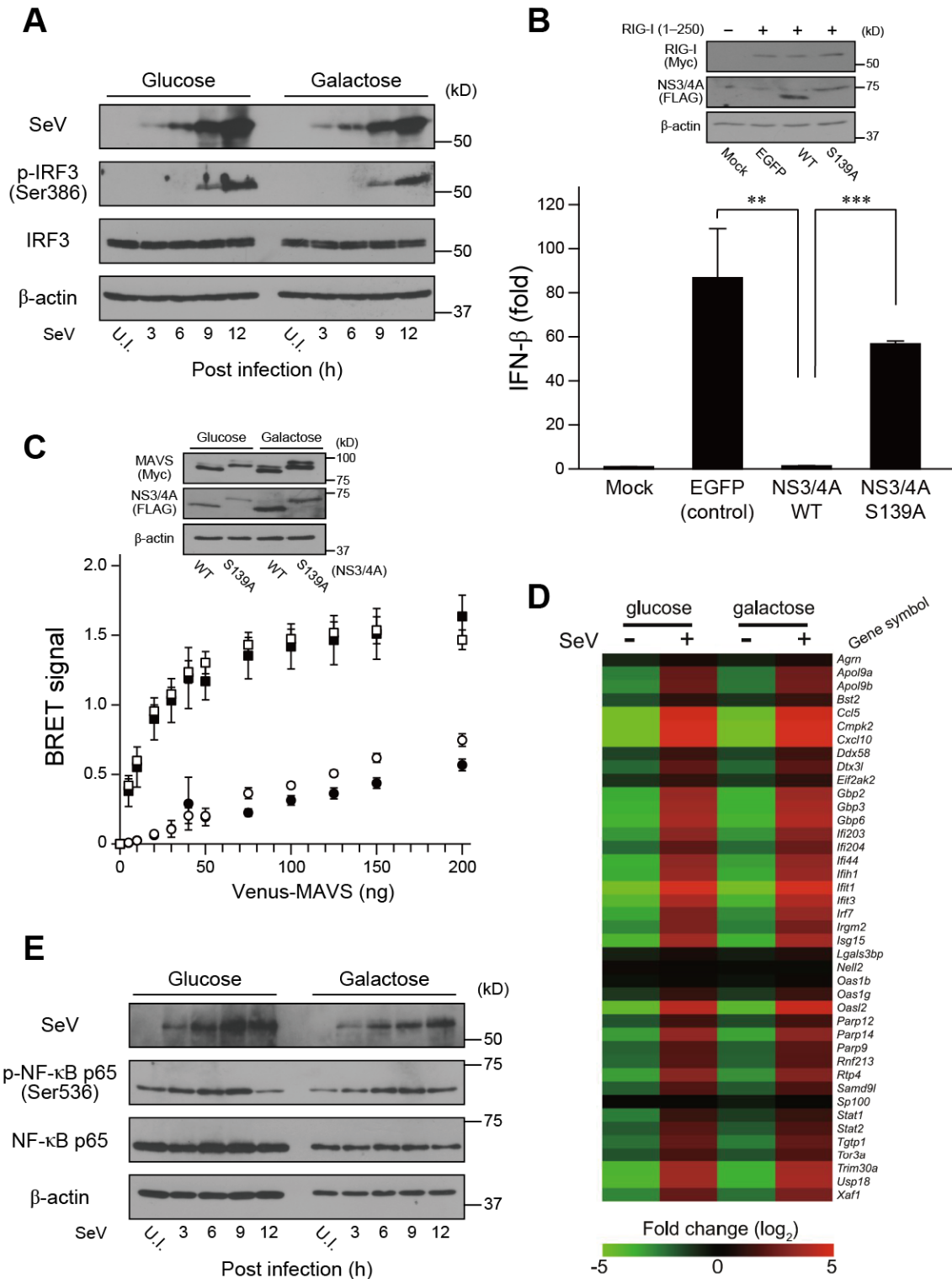


Figure 3

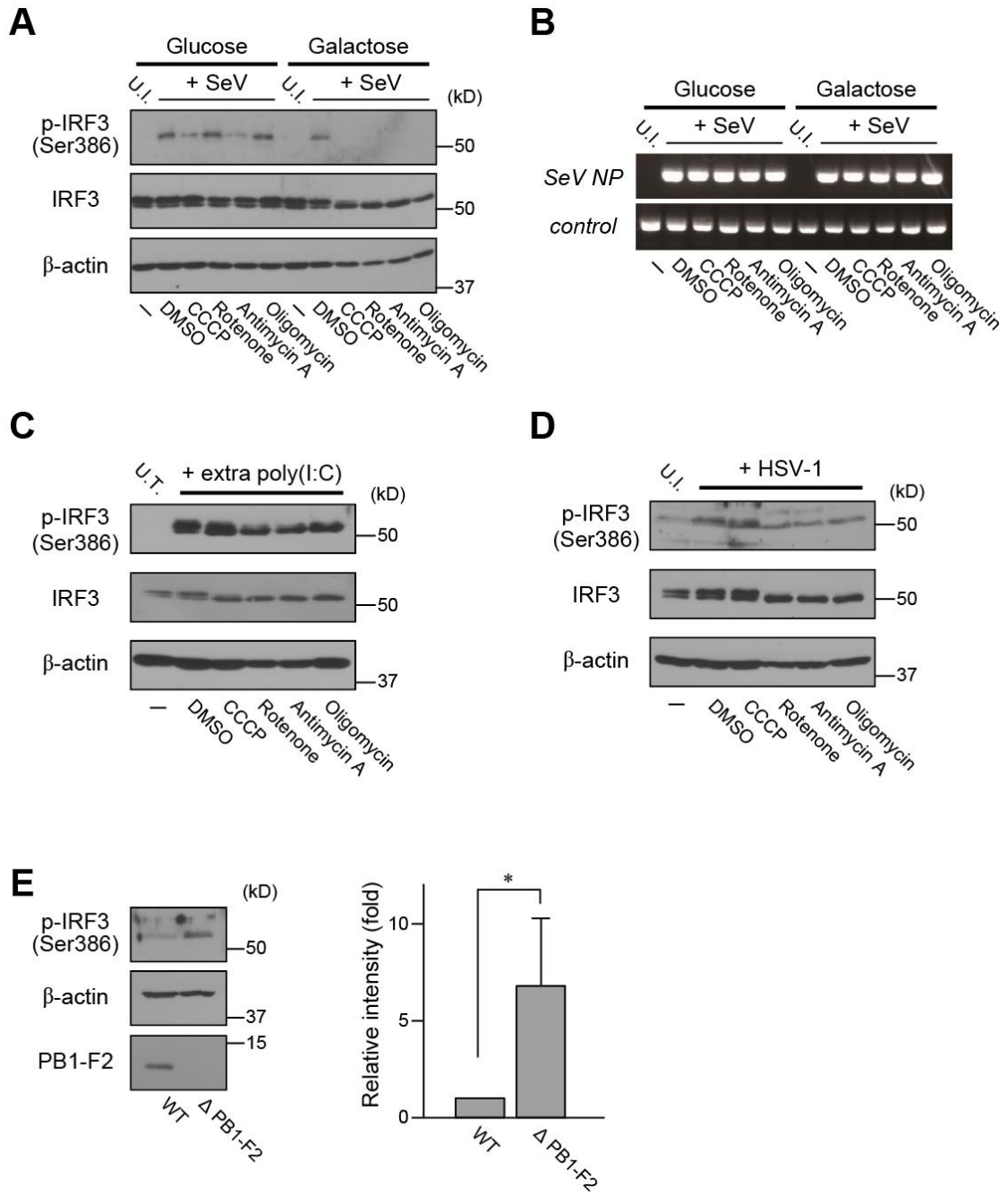


Figure 4

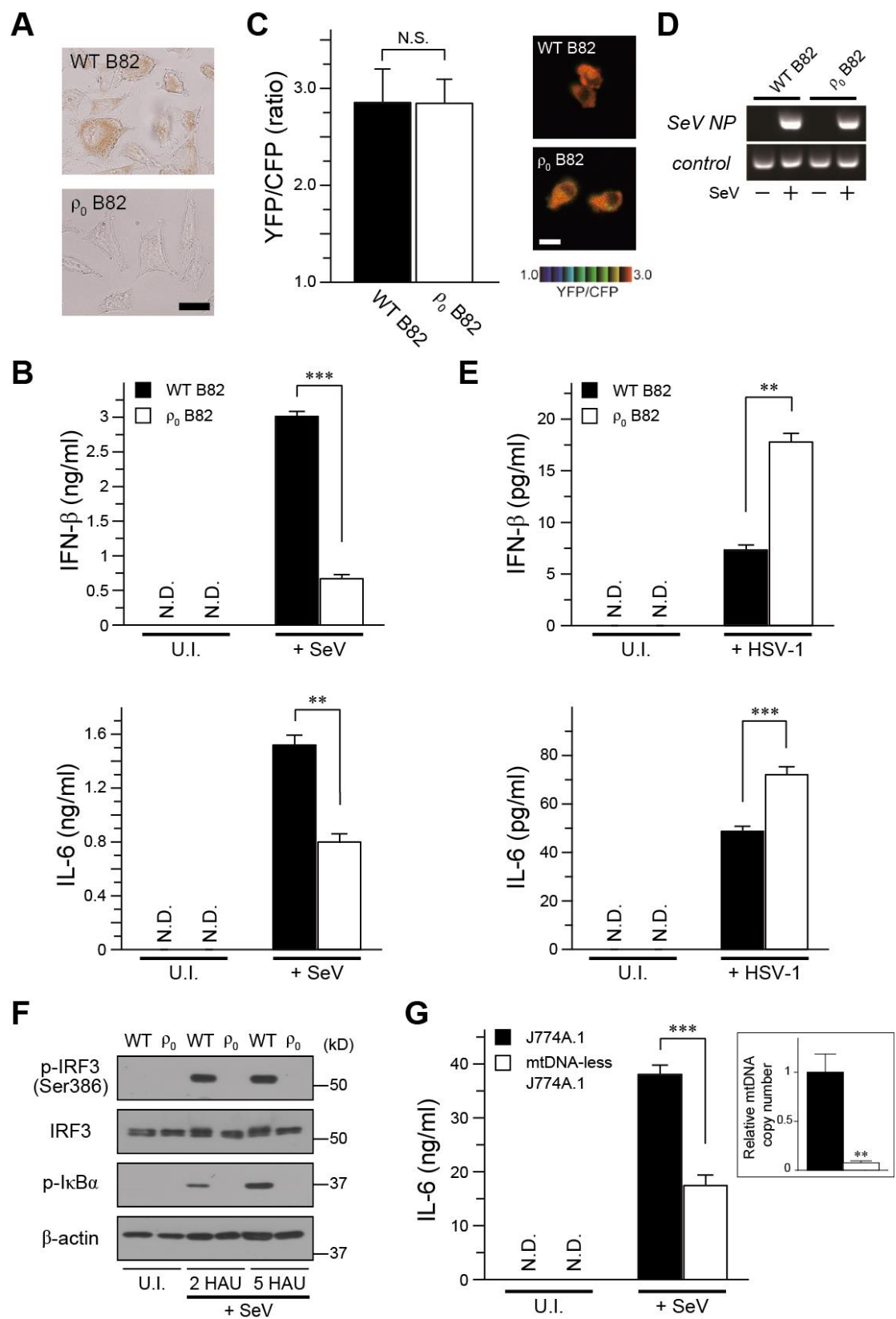


Figure 5

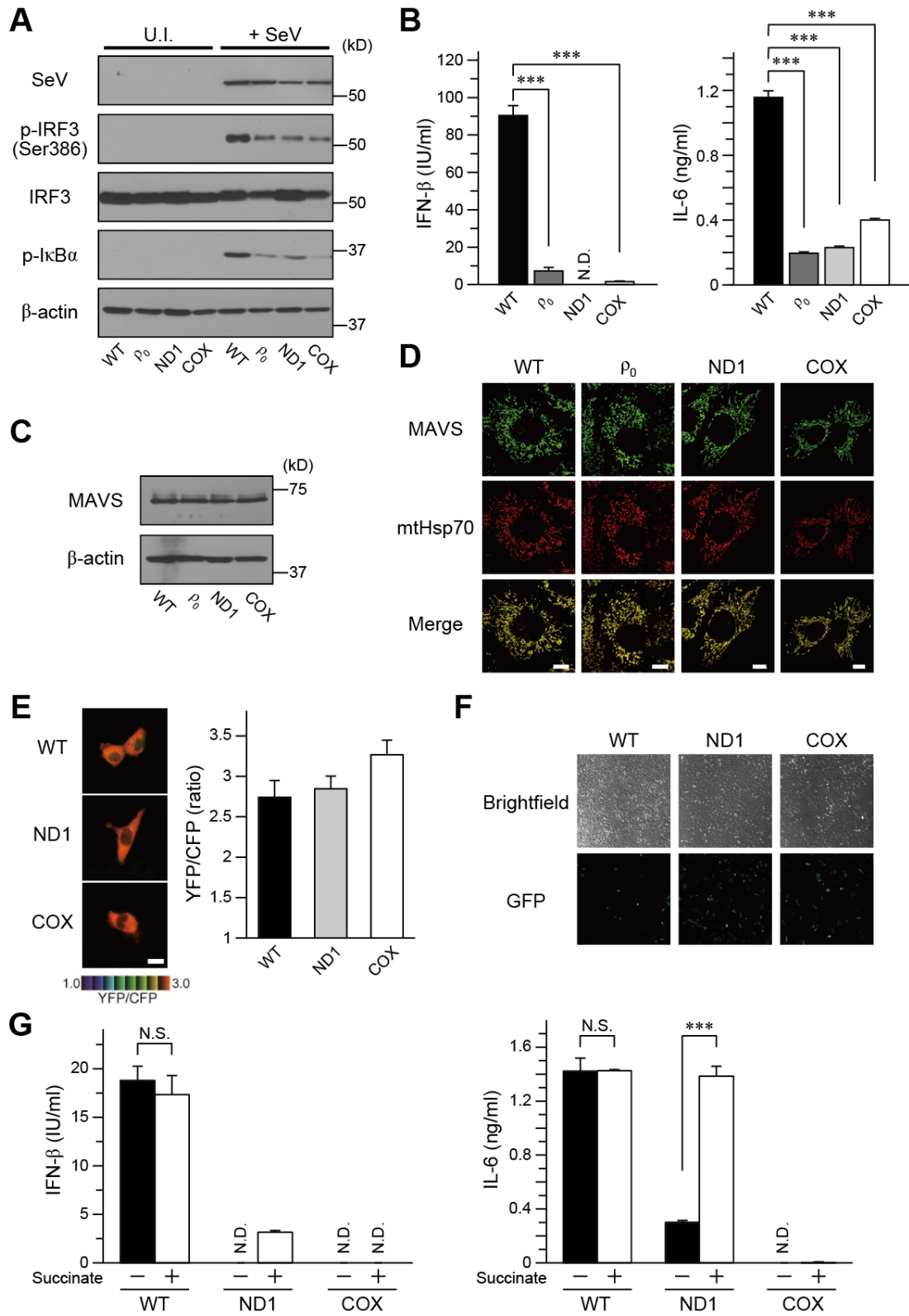


Figure 6

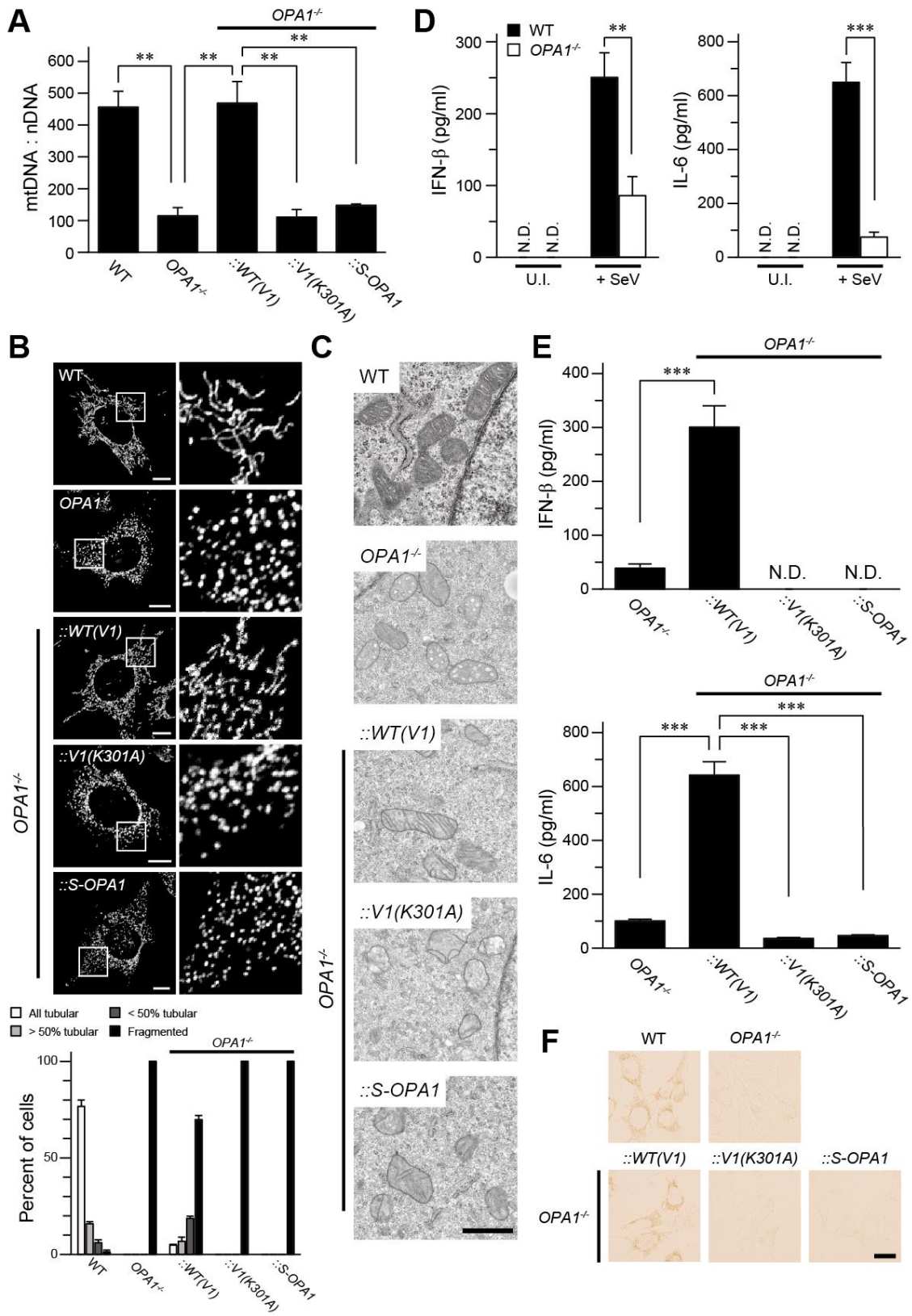


Figure 7